Original Paper

Development of an ultra-high-pressure rotary combined dynamic seal and experimental study on its sealing performance in deep energy mining conditions

Wei Huang [a, b], Gan Feng [a, c, *], Hui-Lan He [d], Jian-Zhong Chen [e], Jiu-Quan Wang [d], Zhao Zhao [f]

[a] Key Laboratory of Deep Earth Science and Engineering (Sichuan University), Ministry of Education, Sichuan University, Chengdu, 610065, Sichuan, China
[b] School of Mechanical Engineering, Sichuan University, Chengdu, 610065, Sichuan, China
[c] College of Water Resource & Hydropower, Sichuan University, Chengdu, 610065, Sichuan, China
[d] Jin Shi Drill Tech Co., Ltd, Tangshan, 063004, Hebei, China
[e] Pingdingshan Tianan Coal Mining Co., LTD., Pingdingshan, 467000, Henan, China
[f] Xi'an Research Institute, China Coal Technology & Engineering Group Corp, Xi'an, 710077, Shaanxi, China

ARTICLE INFO

ABSTRACT

With the continuous development of deep oil and gas, minerals, geothermal resources, and other resources, there are increasingly more stringent requirements for equipment. In particular, the ultra-high-pressure dynamic seals of deep mining device need to be developed. Therefore, considering the use of dynamic seals in unique deep mining environments, an ultra-high-pressure rotating combined dynamic seal was designed and developed and its sealing performance was experimentally measured and analyzed. The results show that the experimental device can operate stably under a pressure of up to 150 MPa and a rotating speed of 76 r/min, and can also operate normally under a rotating speed of up to 140 r/min and a sealing pressure of 120 MPa. During the operation of the ultra-high-pressure rotating combined dynamic seal, the sealing ring does not show obvious damage, which vouches for its sealing performance. No leakage of flow and pressure was detected in the all seal structures within the sealing pressure range of 0–150 MPa. Therefore, the dynamic sealing performance of the device is intact under ultra-high-pressure conditions and can be applied in deep mining environments at a certain depth. The research and development of this device can aid future deep energy exploration and exploitation.

1. Introduction

With the gradual depletion of shallow natural resources, it is inevitable that the energy and resources exploration and exploitation will move to the deeper parts of the earth (Xie et al., 2019; Gao et al., 2021a; Xie et al., 2021). Deep mining is characterized by high in-situ stress, high temperature, and high osmotic pressure (Xie, 2017; Gao et al., 2020a; Gao et al., 2020b). In this complex environment, not only is there a need to explore and understand rock mechanics at depth but there is also a need to stringently test

deep mining devices (Gao et al., 2021b). Xie and Gao et al. developed a visualization technique for studying rock mechanics at depth (Xie et al., 2015). Yin et al. studied the physical and mechanical behavior of rocks subjected to high temperature and revealed the uniaxial compression and shear failure characteristics of rocks (Yin et al. 2021a, 2021b). Gao and Wang et al. carried out in-situ mechanical tests of deep coal and rock and found that the strength of a deep rock mass under engineering disturbance decreases as compared with the conventional triaxial strength (Gao et al., 2020c). Feng et al. studied the mechanical properties and theories of rock fracture, providing basic theories to evaluate the stability of the reservoir and surrounding rock and analyzed the use of efficient mining technology in deep engineering (Feng et al. 2017, 2020). Based on the insufficient pressure-holding capacity of existing sampling equipment, He and Chen et al. developed an in-

---

situ condition-preserved coring (ICP-coring) system and designed a pressure-holding controller based on the Moho square cover principle (He et al., 2019). However, for deep mining devices, the sealing performance, especially the dynamic sealing performance, is critical to ensure smooth and effective operation. During deep drilling, once the sealing structure has problems, it will lead to insufficient drilling pressure, resulting in a long maintenance period, the consumption of a lot of manpower and material resources, and even result in drilling failure.

The sealing performance of devices has been studied by many scholars. Using a three-dimensional simulation model of a sealing ring, Zhu and Cheng concluded that the grooving of the slip ring, the thickness of the slip ring, the compression amount of the O-ring, and the working fluid medium pressure had a significant influence on the contact pressure of the combined sealing ring (Zhu and Cheng, 2017). Guo and Wu et al. used the ANSYS Workbench finite element software to study the influence of the pre-compression ratio of the O-ring, the material hardness of the O-ring, and the thickness of the rectangular slip ring on sealing performance (Guo et al., 2021). Zhao and Suo et al. studied the influence of different surface structures of a rotating combined seal ring on its sealing performance under a maximum pressure of 20 MPa (Zhao et al., 2020). Salant et al. established a calculation model of a reciprocating hydraulic piston seal device to analyze the influence of parameters such as working pressure and sealing ring precompression on the leakage of the reciprocating piston seal (Salant et al., 2007). Nikas and Sayles et al. established a numerical calculation model for the rectangular seals of reciprocating piston rods to study the relationship between sealing pressure and device leakage (Nikas et al., 2006). Chen and Yang et al. used the ABQUS software to analyze the influence of the structural parameters of the sealing ring on the sealing performance of the hat-shaped slip ring combined seal (Chen et al., 2019). Minet and Brunetière et al. developed a lubrication flow model of the main sealing surface by evaluating the roughness of the dynamic sealing surface of the mechanical seal. Based on the cross-coupling differential equation (Minet et al. 2011). Blasiak and Laski et al. calculated the temperature and stress fields of the non-contact seal and studied the influence of different seal structures on seal performance (Blasiak et al., 2013). Mo and Wang et al. analyzed the performance of the reciprocating seal O-ring used in petroleum machinery and found that the maximum contact stress on the main sealing surface presented nonlinear changes with the increase in the moving speed (Mo et al., 2014). Sukumar et al. used the finite element analysis method to reasonably set material and process parameters, which reduced the contact pressure, Mises equivalent stress, and deformation of the sealing interface, and optimized the sealing performance (Sukumar et al., 2015). Based on the cavitation model, Chen and Liu et al. used response surface analysis and other methods to study the influence of the geometric parameters of spiral grooves on the performance of a seal structure and determined the optimal range of each parameter (Chen et al., 2016).

These studies have made significant advancements in the design and development of sealing rings. Most studies, however, have been conducted under conditions of low pressure. In deep mining, due to the great depth (more than thousands of meters) and high in-situ stress, it is difficult to use a low-pressure sealing device. At present, few studies have been conducted on ultra-high-pressure dynamic seals. Therefore, in this study, an ultra-high-pressure rotating combined dynamic seal structure and an experimental system to measure its sealing performance is proposed for use in the deep mining environment. The ultra-high-pressure rotary combined dynamic seal technology is described in detail, an existing and mature sealing ring of model "TG201 special combination sealing ring for mud medium for rod" was selected for the experiment. And the sealing performance of test specimens under different sealing pressures and rotating speeds were carried out. Furthermore, the surface roughness of the two key parts of the sealing device (the main sealing surface and the hydraulic surface) was studied using a 3D contour scanner. Scanning electron microscopy (SEM) was used to observe the microstructural characteristics of these key parts. Therefore, the deterioration of the sealing structure during operation is also studied.

2. Working principle of the rotating combined dynamic seal structure

2.1. Rotating combined dynamic seal structure

The ultra-high-pressure rotating combined dynamic seal consists of three groups of sealing rings, as shown in Fig. 1. Each group of sealing rings consists of an "O" type rubber ring, a "Z" type sealing ring with an inner surface slotted and a supporting spacer, and a "Z" ring made from polytetrafluoroethylene (PTFE). PTFE has the advantages of a low friction coefficient and high wear resistance and can adapt to the working condition of ultra-high-pressure rotary seals. On this basis, a pair of combined grooves were created on the main sealing surface of the "Z" ring matched with the shaft (see Fig. 2).

The function of the composite slot is twofold. On the one hand, due to how the rotating combined sealing ring functions, impurities are brought into the main sealing surface, causing irreparable damage such as scratches or grooves on the sealing surface, which affects the sealing performance. Therefore, a combined groove can be set up to contain impurities and prevent the sealing surface from being damaged. Lubricating oil can also be stored inside the combined groove, and the lubricating oil film can be produced on the main sealing surface during the working process to effectively prevent the wear and damage of the main sealing surface.

The back of the "Z" ring is designed with an arc groove matching that of the "O" ring, which is convenient for the installation and protection of the "O" ring. The "O" ring rubber material has good resilience because of its hyper elastic characteristics, and it gets compressed under the action of hydraulic pressure, thus producing elastic force. The elastic force and the self-sealing force generated under the action of the working fluid medium make the "Z" ring adhere to the surface of the rotating shaft to achieve the sealing effect. The two-stage ultra-high-pressure rotating combined dynamic seal was used in experiments to verify its performance under different pressure and speed conditions to obtain its safety, reliability, and design characteristics.

2.2. "Z" sealing ring performance

The "Z" seal ring is mainly composed of polytetrafluoroethylene (PTFE), which is a thermoplastic molecule with high crystallinity and high molecular weight. Since the main chain of the PTFE molecule is a C-C bond, and fluorine atom replaces all the side bonds, a C-F bond with strong binding energy forms, as shown in Fig. 3. Therefore, PTFE has the advantages of a small friction coefficient, aging resistance, good radiation resistance, high surface viscosity, good self-lubrication performance, etc. However, it also has disadvantages in processing and forming, poor wear resistance, and other shortcomings (Khedkar et al., 2002).

These shortcomings limit the wider use of PTFE. Therefore, composite modification of PTFE has an effective method to improve the properties of PTFE materials. In the composite modification method, we add metal and metal oxides, inorganic materials, and organic materials, etc., to improve the strength, wear resistance, heat resistance, and surface hardness of PTFE.
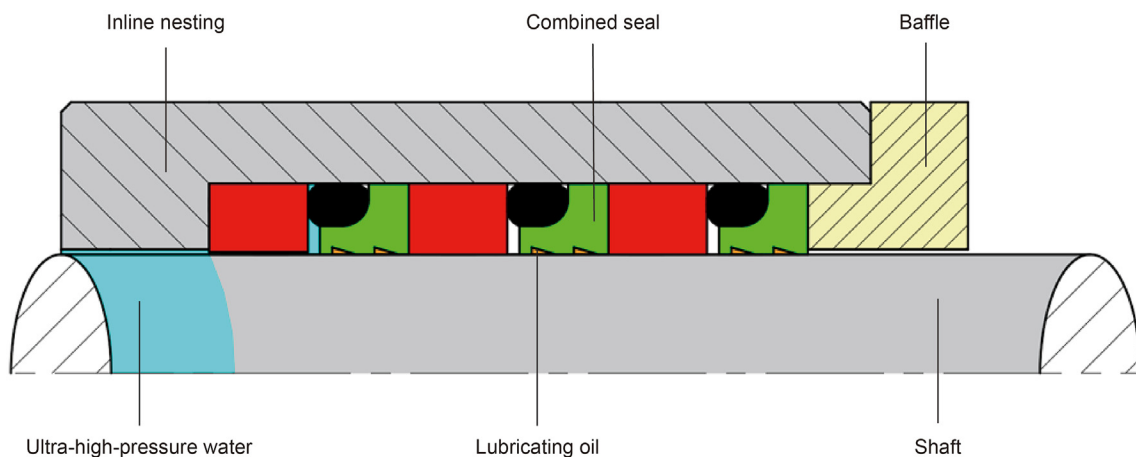
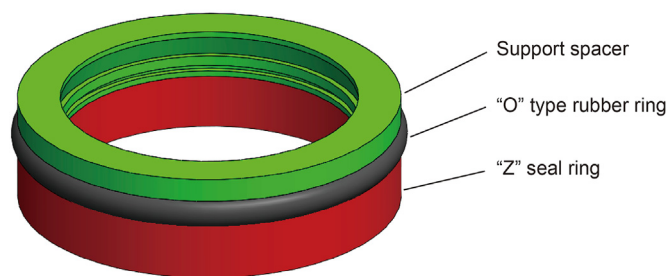**Fig. 1.** Ultra-high-pressure rotary combined dynamic seal structure.

Fig. 2. Structure of the combined seal ring.

2.3. Performance of the "O" type rubber ring

Changes in pressure lead to changes in the characteristics of rubber material, but the volume of the rubber material does not change during deformation. Therefore, rubber is a nonlinear and reversible material. The constitutive relation of rubber is difficult to accurately express because of its nonlinear property. Therefore, its stress-strain curve is assumed to be as shown in Fig. 4.

Rubber is volumetrically incompressible. A substance is considered to be incompressible when its Poisson's ratio is 0.5 or greater than 0.475, i.e. when it is assumed that there is a uniform hydrostatic pressure applied to all the faces of the cell, as shown in Fig. 5. The volume of the element is kept constant continuously, which does not allow for the determination of the compressive

stress of each point inside the element and the strain and joint force of the internal integral points.

Due to the hyper elasticity, nonlinearity, and complexity of the material, the constitutive relation of the "O" type rubber ring cannot be represented by the simple elastic modulus and Poisson's ratio. In 1940, Mooney put forward the theory of large elastic deformation based on Hooke's law (Mooney et al., 1940; Rivlin, 1997); this theory was an important reference for subsequent research on the properties of rubber material. The strain energy function Mooney deduced is:

$$W = C_1 \left(\lambda_1^2 + \lambda_2^2 + \lambda_3^2 - 3 \right) + C_2 \left(1 \Big/ \lambda_1^2 + 1 \Big/ \lambda_2^2 + 1 \Big/ \lambda_3^2 - 3 \right) \tag{1}$$

Where, W is the strain energy density; C_1 and C_2 are material constants; λ_1, λ_2, and λ_3 are the main elongation ratios.

For unidirectional stretching and compression, $\lambda_2^2 = \lambda_3^2 = 1/\lambda_1$, and the following equation can be obtained:

$$W = C_1 \left(\lambda_1^2 + 2 \Big/ \lambda_1 - 3 \right) + C_2 \left(1 \Big/ \lambda_1^2 + 2 \Big/ \lambda_1 - 3 \right) \tag{2}$$

In the case of unidirectional shear strain, $\frac{1}{\lambda_1} = \lambda_3$、 $\lambda_2 = 1$, then

$$W = (C_1 + C_2) \left(\lambda_3^2 + 1 \Big/ \lambda_1^2 - 2 \right) \tag{3}$$

Due to the great limitation of this theory in practical application, Rivlin (Rivlin and Thomas, 1997) expressed the strain energy by
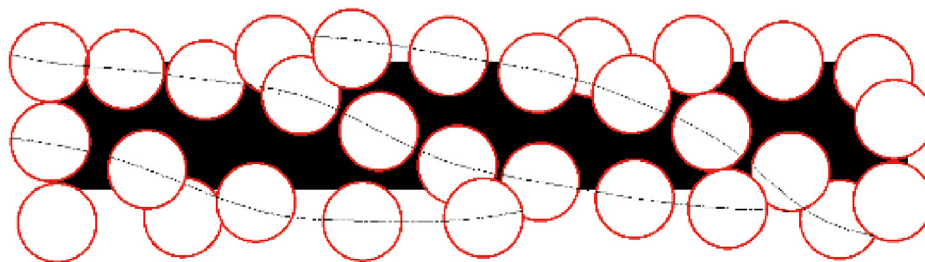

Fig. 3. Polytetrafluoroethylene molecular structure (Zheng et al. 2001)
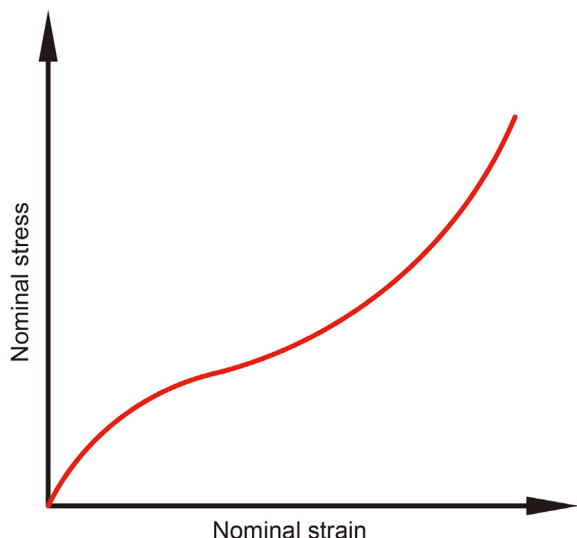
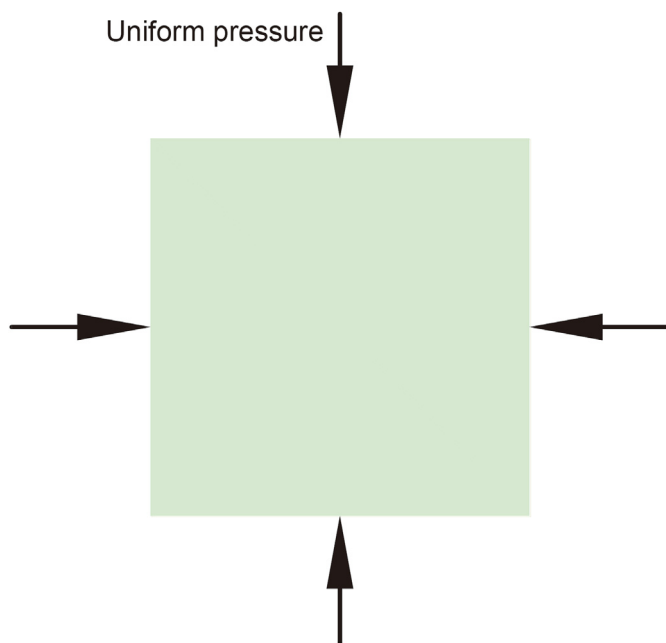**Fig. 4.** Stress-strain curve of rubber (Toki et al., 2013.).

Fig. 5. Unit under uniform hydrostatic pressure (Han, 2019).

using a functional expression composed of strain invariants I_1、I_2, and I_3. The strain energy function is expressed as

$$W = C_{10}(I_1 - 3) + C_{01}(I_2 - 3) \tag{4}$$

Where, C_{10} and C_{01} are the two rubber material parameters that can be determined experimentally, and I_1 and I_2 are the first and second strain invariants, respectively.

Table 1 shows the values of C_{10} and C_{01} under different hardness of rubber materials.

3. Ultra-high-pressure rotary combined dynamic seal test system

3.1. Structure and working principle of the experimental system

To study the performance of the ultra-high-pressure rotating combined dynamic seal, a test system was developed independently. The test system is mainly composed of a rotating combined dynamic seal test kettle, a YY-140 type fidelity coring hydraulic testing platform, a rotary shaft driven pump unit, a hydraulic pipeline, a joint and pressure valve, a flow sensor, etc., as shown in Fig. 6.

The working principle of the ultra-high-pressure rotating combined dynamic seal test system is shown in Fig. 7. The combination of various hydraulic pipeline components in the system completes the application and control of the test pressure in the system. The leakage situation of pipelines at all levels can be understood by observing the pressure gauge, flow meter, and other measuring instruments installed in the pipeline. At the same time, the data acquisition and control system measure the test pressure, flow, and rotation speed of the rotating shaft, and provides real-time recording and display of the measurement data through a computer.

3.2. Rotating combination dynamic seal test kettle

The rotating combined dynamic seal test kettle is the main device used to test the performance of the dynamic seal. The test kettle is mainly composed of a top support reaction cylinder, a top thrust bearing, a rotating shaft, an ultra-high-pressure cabin, a sealing device, and a rotary drive gearbox, as shown in Fig. 8. The reaction force of the piston caused by the hydraulic oil cylinder pressure pushes down on the top of the thrust bearing, which provides a downward thrust to the axis of rotation; the axis of rotation offsets the experimental process by the ultra-high-pressure tank shell at the bottom of the internal water pressure, maintain axial movement in the process of the axis of rotation experiment, can achieve smooth rotation. A rotating shaft is installed inside the ultra-high-pressure cabin body, and self-lubricating bearings, copper sleeves, and other components are set inside the cabin body to achieve the centralization of the rotating shaft and prevent the eccentricity of the rotating shaft. A pressure pulse dissipation pool is set at the bottom of the cabin body to eliminate the liquid pressure fluctuation entering the cabin body through the pressure hole to prevent any damage caused by the pressure pulse to the sealing structure and effectively prevent equipment failure caused by the pressure pulse.

The first and second stage rotating combined dynamic seal structures are respectively composed of a rotating combined seal ring, baffle, and inline nesting. The combined sealing ring is installed inside the inline nesting, and the inline nesting can adjust the mounting size to match the size of the sealing element; this is used to install the sealing element to be tested in different forms and sizes. The rotary drive gearbox is connected to a rotary shaft-driven pump unit through the hydraulic pipeline and drives the rotating shaft to rotate at different speeds according to the experimental requirements. Through the primary and secondary measurement channels, the pressure sensor, speed sensor, flow meter, and other measuring devices are used to record and display the data obtained from the test process.

The ultra-high-pressure cabin body is made of 40Cr material.

Table 1
Rubber material parameters under different hardness (Han, 2019).

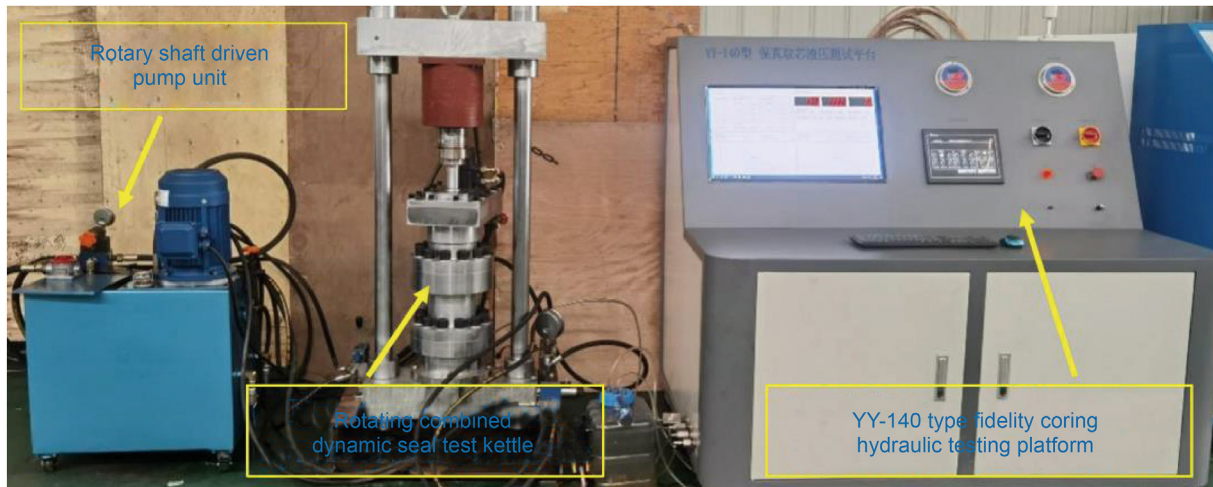| Hr, HA	E, MPa	C_{01}	C_{10}
70	6.96	1.137	0.023
75	8.74	1.444	0.0165
80	10.98	1.833	−0.003
85	13.80	2.334	−0.034
90	17.33	2.972	0.082

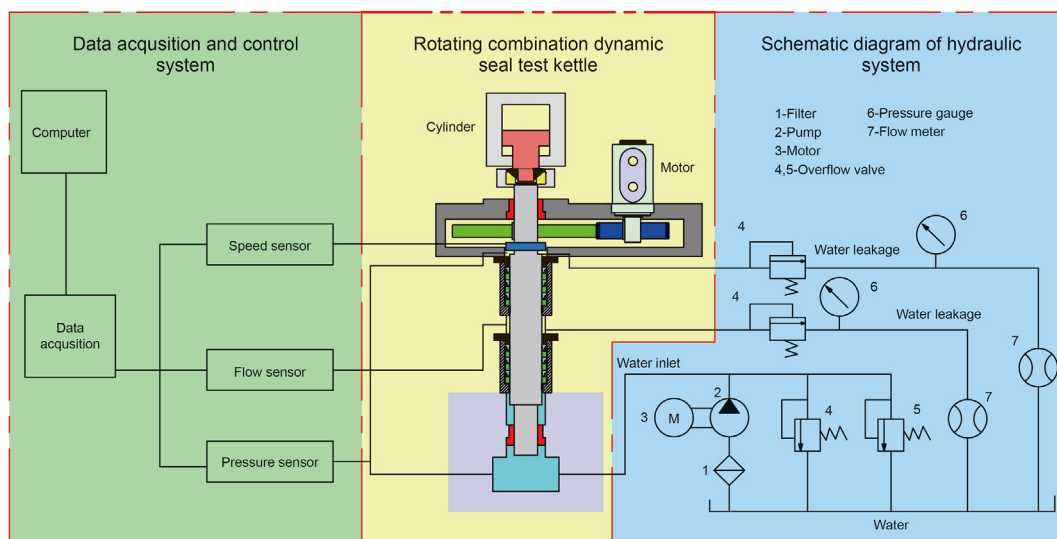**Fig. 6.** Ultra-high-pressure rotary combined dynamic seal test system.

Fig. 7. Schematic diagram of the working principle of the ultra-high-pressure rotary combined dynamic seal test system.

According to the calculation method of the oil cylinder (Cheng, 2010), the wall thickness of the ultra-high-pressure cabin body is 50 mm when the maximum inner diameter is 110 mm, so the minimum wall thickness of the overall cabin is 50 mm. Equation (5) is adopted as the calculation formula (Cheng, 2010).

Cylinder wall thickness is:

$$\delta = \delta_0 + c_1 + c_2 \tag{5}$$

In the formula, C_1-the tolerance allowance of the cylinder's outer diameter, m; C_2-corrosion allowance, m.

The value of δ_0 needs to be calculated according to different situations (Cheng, 2010). The calculation formula of δ_0 under three scenarios is as follows:

(1) When $\delta/D \le 0.08$, the practical calculation formula for cylinder wall thickness is as follows:

$$\delta_0 > \frac{P_{max}D}{2\sigma_P} \ (m) \tag{6}$$

(2) When $0.08 \le \delta/D \le 0.3$

$$\delta_0 > \frac{P_{max}D}{2.3\sigma_P - 3P_{max}} \ (m) \tag{7}$$

(3) When $\delta/D > 0.3$

$$\delta_0 > \frac{D}{2}\left(\sqrt{\frac{\sigma_P + 0.4P_{max}}{\sigma_P - 1.3P_{max}}} - 1\right)(m) \tag{8}$$

or

$$\delta_0 > \frac{D}{2}\left(\sqrt{\frac{\sigma_P}{\sigma_P - \sqrt{3}P_{max}}} - 1\right)(m) \tag{9}$$

In the above formula, D-inner diameter of the cylinder, m; P_{max}-the maximum working pressure in the cylinder, MPa; σ_P-allowable stress of the cylinder material, MPa; -tensile strength of the cylinder material, MPa; n-safety factor, usually n=5; can also be selected according to
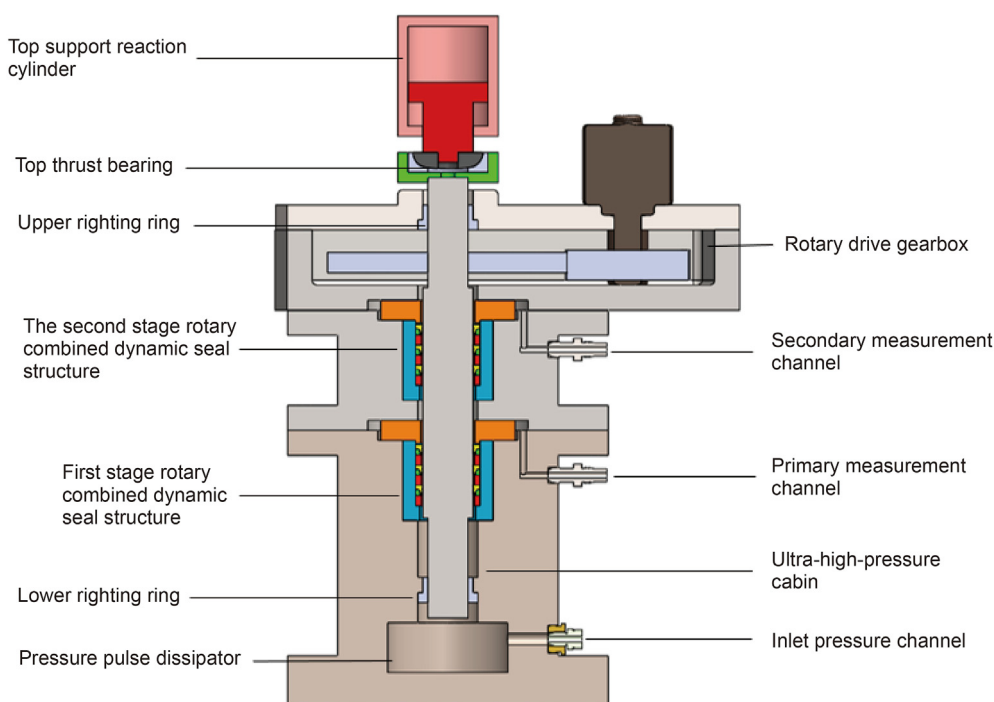
Fig. 8. Rotating combined dynamic seal test kettle.

the actual situation; In this experiment, 3.6 can meet the requirements.

3.3. YY-140 type fidelity coring hydraulic testing platform

The YY-140 type fidelity coring hydraulic testing platform consists of an automatic pressurization system and a manual pressurizing system, as shown in Fig. 9. The automatic pressurization system can record pressurization pressure and flow curve in real-time, but it takes a long time to apply the pressure. To quickly realize the application of high pressure, a manual pressure system was set, but the curve of the pressure change and flow was not recorded during the process of manually applying the pressure. The test platform can provide up to 190 MPa of hydraulic pressure. The test platform integrates data acquisition, display, and data processing. During the test of the ultra-high-pressure rotating combined dynamic seal, the pressure and flow inside the ultra-high-pressure cabin were collected and displayed in real-time, and the rotation speed of the rotating shaft was also simultaneously displayed.

The platform uses mechanical, electrical, hydraulically-integrated control technology, a numerical control technology algorithm, automatic feedback from the computer, and closed-loop control stability pressure. The entire system includes two sets of high-precision servo-controlled thrust oil sources (as shown in Fig. 10), with characteristics of infinite total volume pressurization and pressure stabilization.

The loading of the thrust oil source structure was performed using the computer automatic control system. The computer automatic control system collects the pressure value of each hydraulic section and compares it with the upper and lower limits of the preset pressure of each section; it then instructs the Programmable Logic Controller (PLC) to automatically control the motor and battery valve of each hydraulic section. If the pressure gauge value of the pressure holding vessel is lower than the lower preset pressure limit, the system automatically instructs the PLC to start

Fig. 9. Schematic diagram of the YY-140 type fidelity coring hydraulic test platform.

the oil pump motor, and when the pressure is higher than the upper limit, the motor will stop automatically. When the containment vessel needs to be pressurized, the solenoid valve opens automatically to provide sufficient pressure. The solenoid valve closes automatically when the pressure holding vessel reaches the set pressure value. The reciprocating cycles of each hydraulic section constitute the pressurized and stabilized hydraulic circuit of the container to realize the automatic pressurization and pressure stabilization of the container. At the same time, the oil pump motor in the automatic system does not need to run for a long time, and, therefore, the automatic system has the advantages of energy-saving, low noise, and long service life of the oil pump motor.
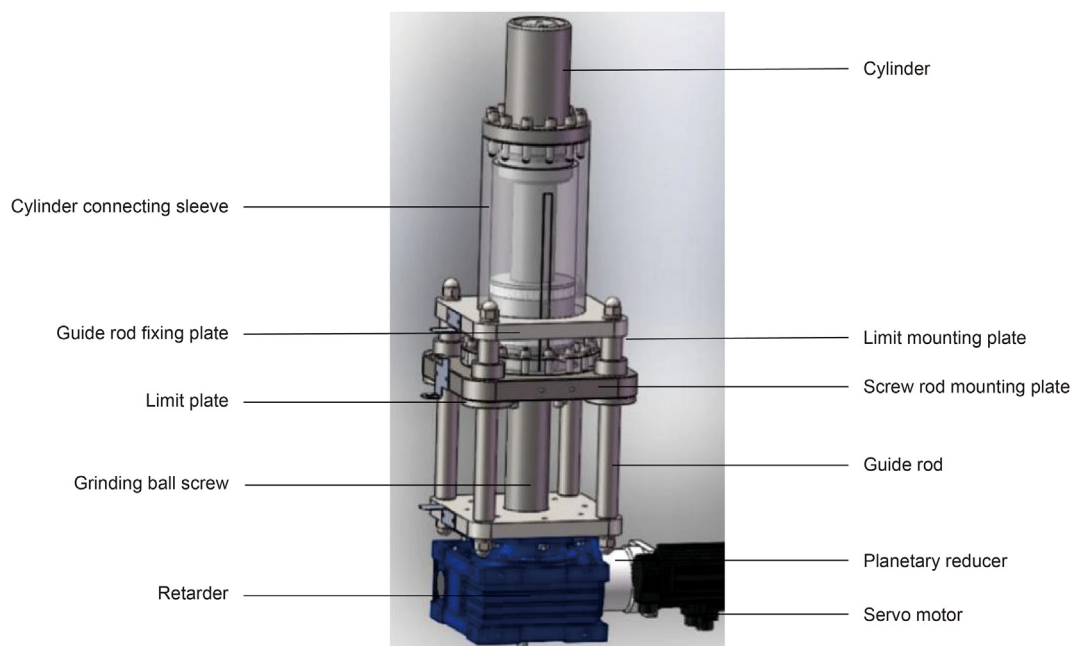
Fig. 10. Schematic diagram of the single acting thrust oil source.

4. Ultra-high-pressure rotating combination dynamic seal test

4.1. Experimental procedures

To test the performance and sealing reliability of the dynamic seal structure, different maximum sealing pressures were applied to the dynamic seal structure in the experimental system. The three sets of maximum sealing pressure were 110 MPa, 140 MPa, and 150 MPa. Sealing performance tests were carried out in stages according to the order of pressure. The diameter of the rotating shaft was designed to be 50 mm. The pressure sensor and flow sensor were installed after the first and second stage seal structures to monitor the leakage pressure and flow rate of the seal structures in real-time; these are considered as the main measurement index of the sealing structure's performance.

The specific experimental process is as follows:

(1) Sealing performance test with a maximum sealing pressure of 110 MPa. First, we filled the pressure pulse dissipator with water. Then, the rotating shaft was made to run at 120 r/min. Finally, the automatic pressure system of the YY-140 type fidelity coring hydraulic test platform was activated step by step to increase the pressure inside the pressure pulse dissipating pool to 110 MPa.

(2) Sealing performance test with a maximum sealing pressure of 140 MPa. To test the performance of the sealing structure at different rotating speeds, three groups of rotating speeds were set for the loading experiments. ① The pressure inside the pressure pulse dissipating pool was rapidly increased to 108 MPa by the manual pressurization system, and then the rotating shaft was run at a speed of 100 r/min. Then, the pressure was gradually increased to 140 MPa by the automatic pressurization system, and the speed was adjusted to 64 r/min. ② The pressure was adjusted to 120 MPa and the speed was increased to 120 r/min to carry out the experiment. ③ The pressure was then increased to 140 MPa and the speed was increased to 136 r/min. Sensor data of leakage

pressure and leakage flow, as well as voltage stabilization time, were recorded throughout the experiment.

(3) Sealing performance test with the maximum sealing pressure of 150 MPa. After the internal pressure of the pressure pulse dissipating pool was rapidly increased to 135 MPa by manual pressurization, the rotating shaft was run at a speed of 76 r/min, and then the pressure was increased to 150 MPa by the automatic pressurization system. Sensor data of leakage pressure and leakage flow, as well as voltage stabilization time, were recorded throughout the experiment.

5. Results and analysis

5.1. Maximum sealing pressure of 110 MPa

During the experiment, due to the system balance lag, there was a difference between the actual value and the set value. Typical pressure value data were recorded, and the actual measured value corresponding to the set value is as shown in Table 2.

In this experiment, by injecting water into the device to compress the volume, the bearing pressure of the sealing structure was exerted. Therefore, once the sealing structure was unstable, it caused pressure leakage (leakage pressure) and water leakage (leakage flow rate). The data of leakage pressure and leakage flow during the experiment were obtained through an automatic recording by a computer. For convenient analysis and visualization, all the above data are plotted into curves, as shown in Fig. 11 below.

It can be seen from Fig. 11 that with the continuous increase in the water intake, the sealing pressure gradually increases, and the rotational speed remains constant at 120 r/min. When the pressure value exceeds 60 MPa, the speed decreases automatically as the sealing pressure increases. When the sealing pressure reaches 110 MPa, the speed decreases to 112 r/min, which is 6.7% lower than the set value. This is because the rotating shaft cannot rotate absolutely smoothly, and, therefore, the increase in the sealing pressure increases the operating torque of the rotating shaft, thus creating frictional resistance that hinders the rotation of the rotating shaft. It was observed that the speed decline rate remained

constant at a rate of 0.2 r/min/MPa, indicating that the pressure-speed operation of the sealing structure was stable. During the rise in the sealing pressure, the pressure was recorded for 3–5 min at the set typical pressure value. During the entire experiment, the leakage pressure value was 0, and the leakage flow value was 0. This indicates that under 110 MPa pressure and 112 r/min speed, the rotating combined dynamic seal structure has good sealing performance and operates stably.

5.2. The maximum sealing pressure of 140 MPa

Since the rotating combined dynamic seal structure showed good running condition in the preliminary experiment, the maximum sealing pressure was increased to 140 MPa to further test the seal's structure. Since the sealing pressure causes resistance to the operation of the rotating shaft, that is, the sealing pressure is negatively correlated with the speed, different rotating speeds were set to perform the sealing performance experiments.

5.2.1. Performance at 64 r/min under ultra-high-pressure

The water flow rate was rapidly increased to increase the sealing pressure to 120 MPa, and the pressure was stabilized for 5 min. The rotation speed of the rotating shaft was set at 100 r/min. The parameters recorded during the experiment are shown in Table 3.

As can be seen from Table 3, under the ultra-high-pressure of 140 MPa, there is a difference between the actual sealing pressure and the set value, but the difference is so small that it can be almost ignored. It should be noted that the pressure remained constant for 14 min under the ultra-high-pressure condition. This shows that the pressure control experiment of the rotary combined dynamic seal system designed in this paper is highly precise. To directly reflect the parameters and leakage situation during the experiment, the data were drawn into curves, as shown in Fig. 12.

As shown in Fig. 12, with the step-by-step increase in the water intake, the sealing pressure increases accordingly. When the pressure is 120 MPa, the speed is 100 r/min and decreases to 64 r/min with the increase in the pressure to 140 MPa. The reduction rate is 1.8 r/min/MPa. This reduction rate is significantly higher than the 0.2 r/min/MPa in the 60–110 MPa high-pressure range. Therefore, when the pressure exceeds 110 MPa, the influence of the increase in the pressure on the speed is very obvious. This is also due to the increased resistance caused by the pressure of the shaft. It was observed that there was no water leakage under the 120 MPa and 130 MPa sealing pressure conditions. When the pressure was increased to 140 MPa, the leakage pressure and leakage flow value were still 0 after 14 min of stable pressure. Therefore, under an ultra-high-pressure of 140 MPa and a rotating speed of 64 r/min, the sealing performance of the rotating combined dynamic seal structure is good.

5.2.2. Performance at 125 r/min under ultra-high-pressure

To explore the sealing performance at higher rotating speeds

under ultra-high-pressure conditions, performance test experiments were carried out at rotating speeds above 120 r/min. Under an initial manual pressure of 100 MPa, the water intake was not measured. The experimental parameter data are shown in Table 4.

When the pressure is increased to 120 MPa with a gradient of 20 MPa, the speed decreases to 133 r/min, and the system runs stably after 1 min of voltage stabilization. When the pressure was increased to 140 MPa with a gradient of 20 MPa, the speed reduced to 125 r/min, and the pressure stabilization time was 7 min. The data in the table and the sensor data recorded in the experiment were plotted on curves for observation and analysis, as shown in Fig. 13.

As can be seen from Fig. 13, with a set speed of 136 r/min and a pressure boost interval of 100-120 MPa, the average decrease in the gradient of the speed with the increase in the pressure is 0.15r/min/MPa. This is obviously lower than the initial setting of 0.2 r/min/MPa in the high-pressure range of 120 r/min and 60–110 MPa. Therefore, at high speed, the inhibiting effect of the increase in pressure is relatively weak, that is, increasing the initial speed within a certain pressure range can reduce the weakening effect of the pressure increase on the speed.

The average speed decrease gradient is 0.4r/min/MPa in the 120-140 MPa pressure boost interval, which is higher than 0.15r/min/MPa in the 100-120 MPa pressure boost interval. Combined with the analysis of the speed vs sealing pressure curve in Fig. 13 (c), it can be concluded that when the pressure exceeds 100 MPa, the increase in pressure causes an increase in the friction force, which leads to a quicker decrease in the speed.

Comparing the stabilizing time of 14 min at the speed of 64 r/min under the ultra-high-pressure of 140 MPa with the stabilizing time of 7 min at the speed of 125 r/min under the ultra-high-pressure of 140 MPa shows that the stabilizing time of the system reduces by increasing the speed under the same pressure. Meanwhile, during the entire experiment, it was observed that the value of the leakage pressure and the leakage flow remained at 0. Therefore, under conditions of an ultra-high-pressure of 140 MPa and a rotating speed of 125 r/min, the sealing performance of the rotating combined dynamic seal structure is good.

5.2.3. Performance at a speed of 140 r/min under ultra-high-pressure

To further test the performance of the ultra-high-pressure sealing structure at a higher speed, the speed was directly increased to 140 r/min and the pressure was reduced to 120 MPa. While initially setting the manual pressure to 120 MPa, the water intake was not recorded. Parameter details during this experiment are shown in Table 5.

For intuitive understanding, the table data and the sensor data recorded in the experiment were also drawn into curves, as shown in Fig. 14.

As shown in Fig. 14, the experiment was carried out at a high speed of 140 r/min for a stabilizing time of 3.5 min. Under ultra-

Table 2
Experimental parameters of test with the maximum sealing pressure of 110 MPa.

Set sealing pressure, MPa	Actual sealing pressure, MPa	Actual speed, r/min	Holding time, min
0	0	120	0
30	30.05	120	5
60	60.05	120	3
70	69.95	118	3
80	79.90	114	3
90	89.93	116	3
100	99.85	114	3
110	109.91	112	5

(a) Accumulated water inflow vs time

(b) Sealing pressure vs time

(c) Speed vs sealing pressure

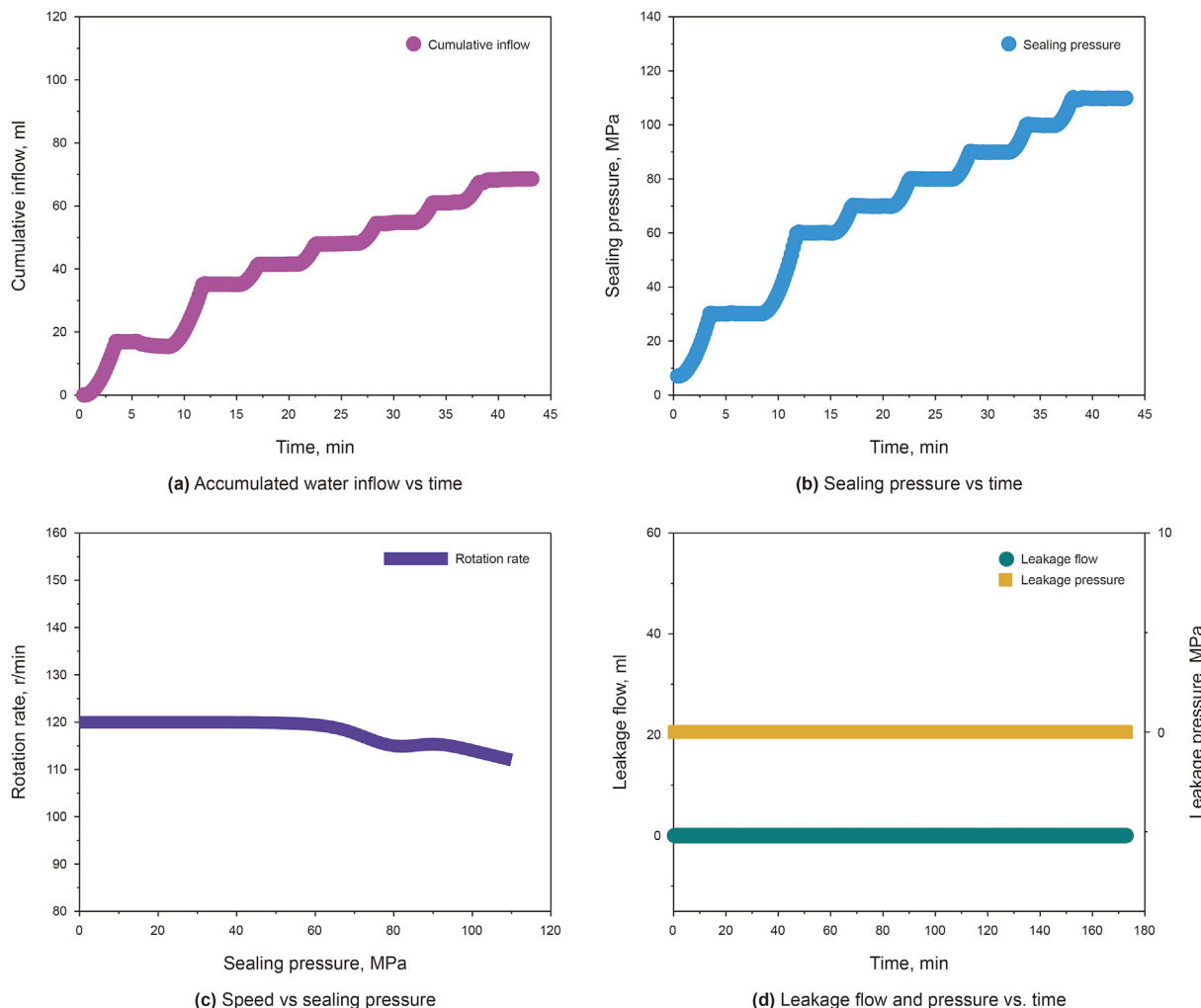**(d)** Leakage flow and pressure vs. time

Fig. 11. Curve of the experimental parameters and results (maximum sealing pressure of 110 MPa).

Table 3
Performance test parameters at 64 r/min speed.

Set sealing pressure, MPa	Actual sealing pressure, MPa	Actual speed, r/min	Holding time, min
120	120.10	100	5
130	129.95	74	5
140	139.94	64	14

high pressure, the increase in the pressure and speed result in significant heat generation, which causes the system pressure to fluctuate and shortens the time of pressure stabilization. Therefore, if the speed is increased again, the voltage stabilizing time will reduce. The stabilizing time can be increased by further reducing the pressure to below 120 MPa. In contrast, the stabilizing time is 14 min at a speed of 64 r/min at 140 MPa. This shows that the stabilizing time can be significantly improved by increasing the pressure and decreasing the rotational speed. During the experiment, the experimental data of leakage pressure and leakage flow were continuously recorded, and their values consistently remained at 0. Therefore, under an ultra-high-pressure of 120 MPa and a rotating speed of 140 r/min, the rotating combined dynamic seal structure has good sealing performance.

5.3. The maximum sealing pressure of 150 MPa

It is very difficult to create a dynamic seal that functions well under ultra-high pressure. However, in this study, we found that the maximum sealing pressure of the ultra-high-pressure rotary combined dynamic seal can be increased. Therefore, we decided to test the dynamic seal under a maximum sealing pressure of 150 MPa. The experimental parameters are shown in Table 6.

It can be seen from Table 6 that the actual sealing pressure is almost the same as the set ultra-high-pressure of 150 MPa. This provides further verification that the precision of the pressure control system in our experimental setup is very high. As done previously, experimental data in the table and the experimental data recorded from the first and second stage seal structures were drawn into curves, as shown in Fig. 15.
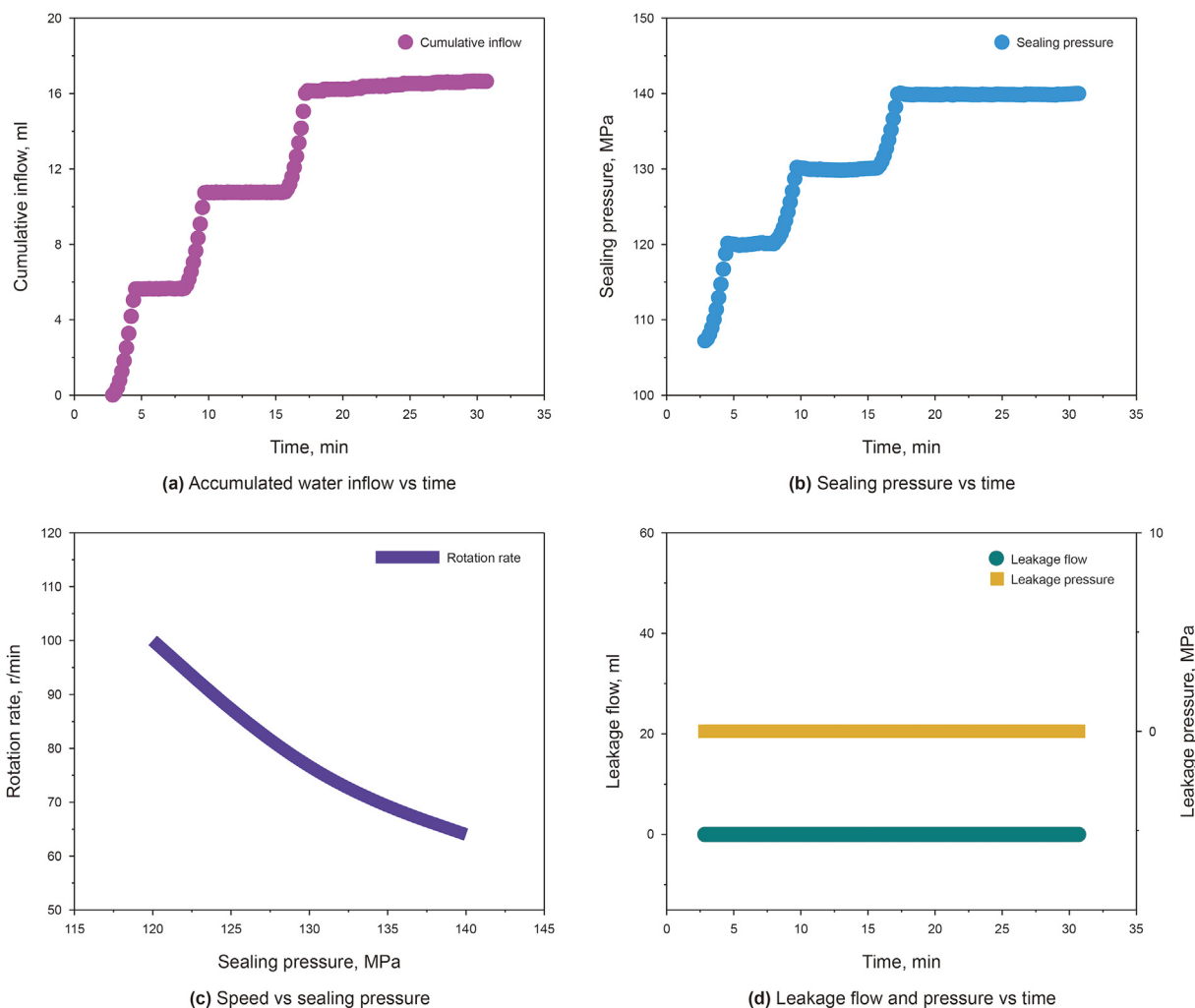
(a) Accumulated water inflow vs time

(b) Sealing pressure vs time

(c) Speed vs sealing pressure

(d) Leakage flow and pressure vs time

Fig. 12. Experimental parameters and result curve (maximum sealing pressure 140 MPa).

Table 4
Performance test parameters at 125 r/min.

Set sealing pressure, MPa	Actual sealing pressure, MPa	Actual speed, r/min	Holding time, min
100	100.00	136	2
120	120.01	133	1
140	139.95	125	7

As can be seen from Fig. 15, the stability time reached 16 min under 150 MPa. This is an increase in the stabilization time achieved by reducing the speed under ultra-high pressure. At the same time, the leakage pressure and leakage flow recorded during the first and second stages were 0; this indicates that the sealing performance of the rotating combined dynamic seal structure is good under an ultra-high pressure of 150 MPa and a rotating speed of 76 r/min. From the above research results and trend analysis, if further design experiments reduce the speed, it can continue to increase the seal pressure. Therefore, in this study, it was found that the newly designed and developed rotating combined dynamic seal has good sealing performance under ultra-high pressure, and solves the problem of dynamic seal.

6. Wear analysis

One of the key requirements of deep equipment is that the ultra-high-pressure rotary combined dynamic seal structure should exhibit excellent wear resistance. The wear condition of the key contact parts between the sealing ring and the rotating shaft is related to the wear resistance, sealing life, and operational reliability of the sealing structure. In recent years, many studies have reported on the tribological properties of different tribopairs under normal pressure conditions (Wood, 2017; Chen and Cai, 2019; Zhao et al., 2019). However, under the action of ultra-high-pressure sealing pressure, the torque of the rotating shaft increases to form friction resistance. At the same time, the side of the sealing
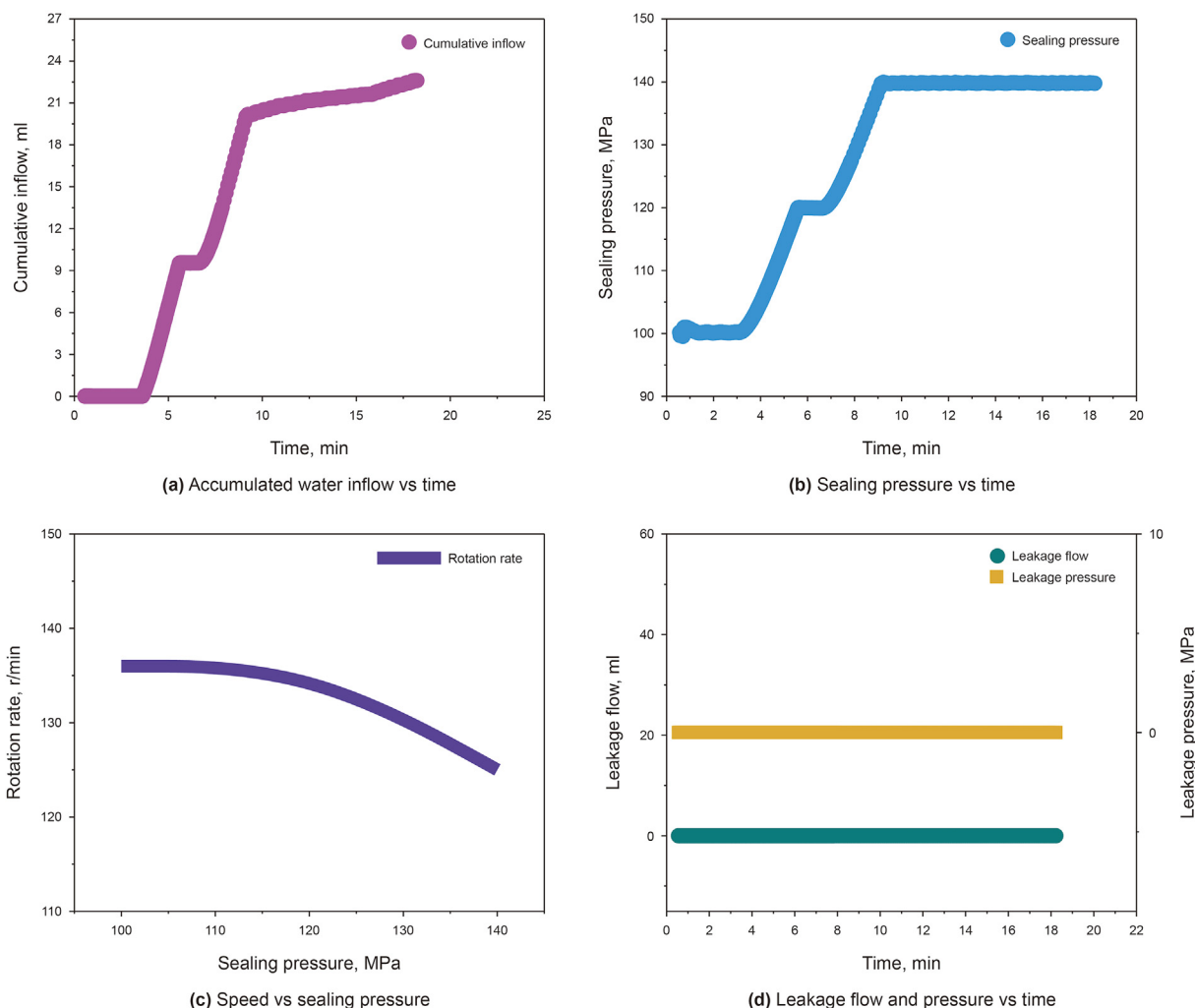
(a) Accumulated water inflow vs time

(b) Sealing pressure vs time

(c) Speed vs sealing pressure

(d) Leakage flow and pressure vs time

Fig. 13. Experimental parameters and result curve (maximum sealing pressure of 140 MPa and a rotating speed 125 r/min).

Table 5
Performance test parameters under 140 r/min speed.

Set sealing pressure, MPa	Actual sealing pressure, MPa	Actual speed, r/min	Holding time, min
120	119.95	140	3.5

ring is subjected to ultra-high water pressure, which causes wear and tear. Therefore, in the section below, the wear of the main sealing surface and the hydraulic surface of the "Z" type sealing ring is analyzed.

6.1. Three-dimensional scanning morphology analysis of the main sealing and hydraulic surfaces

6.1.1. Three-dimensional scanning morphology analysis of the main sealing surface

The main sealing surface is the part where the sealing ring is in direct contact with the rotating shaft. The surface topography of the main sealing surface before and after the experiment was observed using a 3D contour scanner. Before the experiment, the main sealing surface was scanned in three dimensions and its surface topography was recorded. After performing the ultra-high-pressure rotating combined dynamic seal experiment, the main sealing surface was scanned again in the same area. Because the sealing

ring presents a certain circular shape, it should be scanned as straight as possible. The experimental results and sealing ring samples obtained by the 3D scanning test are shown in Fig. 16.

Fig. 16 shows that the sealing ring shows certain wear before and after the experiment, some of which are on the contact surface between the sealing ring and the rotating shaft, indicating that the morphology has changed. The surface parameters were extracted from the surface topography obtained by 3D scanning to quantitatively measure the wear condition. We selected a typical area and calculated its surface topography parameters. The following calculation formula is quoted from the references (ISO, 2012).

The surface character parameter S_a represents an arithmetic mean of the absolute of the ordinate values within a defined area. Formula (10) is as follows:

$$Sa = \frac{1}{A} \iint\limits_{A} |z(x,y)| dxdy \tag{10}$$

(a) Accumulated water inflow vs time

(b) Sealing pressure vs time

(c) Speed vs sealing pressure

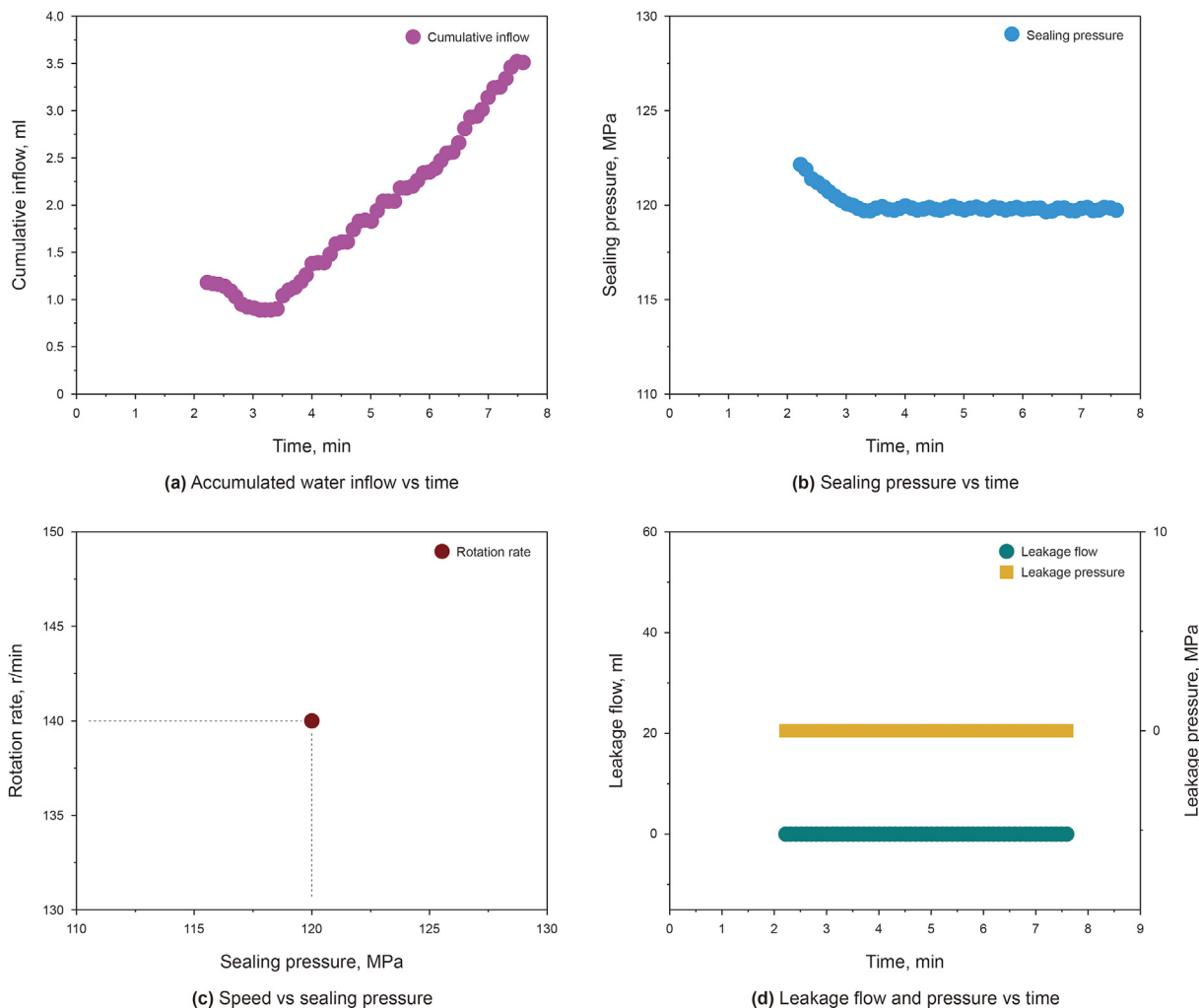**(d)** Leakage flow and pressure vs time

Fig. 14. Experimental parameters and result curves (maximum sealing pressure of 120 MPa and a rotating speed 140 r/min).

Table 6
Experimental parameters of the maximum pressure of 150 MPa.

Set sealing pressure, MPa	Actual sealing pressure, MPa	Actual speed, r/min	Holding time, min
150	149.99	76	16

S_z represents the sum of the maximum peak height value and the maximum pit height value within a defined area. S_{tr} represents the texture aspect ratio. It is calculated by Formula (11).

$$S_{tr} = \frac{\min\limits_{t_x,t_y \in R} \sqrt{t_x^2 + t_y^2}}{\max\limits_{t_x,t_y \in Q} \sqrt{t_x^2 + t_y^2}} \quad where \ R = \left\{ (t_x, t_y) : f_{ACE}(t_x, t_y) \leq s \right\}$$

$$Q = \left\{ (t_x, t_y) : f_{ACE}(t_x, t_y) \geq sand** \right\}$$

(11)

S_{pc} represents the arithmetic mean of the principal curvatures of peaks within a defined area. It is calculated by Formula (12).

$$S_{pc} = \frac{1}{2} \frac{1}{n} \sum_{k=1}^{n} \left(\frac{\partial^2 z(x,y)}{\partial x^2} + \frac{\partial^2 z(x,y)}{\partial y^2} \right)$$

(12)

The calculated results were averaged and are shown in Table 7. As can be seen from Table 7, the surface roughness Sa changed from 6.925 μm before the experiment to 1.945 μm after the experiment. Therefore, the rotating dynamic seal experiment significantly reduced the roughness of the sealing ring. After the experiment, the sealing ring became smooth because the cylindrical surface outside the rotating shaft is smoother than the main sealing surface, and, therefore, the sealing ring became polished under ultra-high-pressure and high-speed rotation.

Another wear phenomenon observed of the sealing ring before and after the experiment was the change in the depth of the oil groove. After the dynamic seal test, the depth of the oil groove became shallower. However, the oil groove was filled with lubricating oil to lubricate the sealing ring when in contact with the rotating shaft. The wear of the contact surface leads to the decrease of the volume of the oil groove. If the oil groove becomes smaller for a long time, it will lead to a lack of lubrication between the sealing ring and the rotating shaft, which will affect the rotation of the rotating shaft.

It can be seen that under ultra-high pressure, the sealing ring is not only worn smooth by the outer cylinder of the rotating shaft but
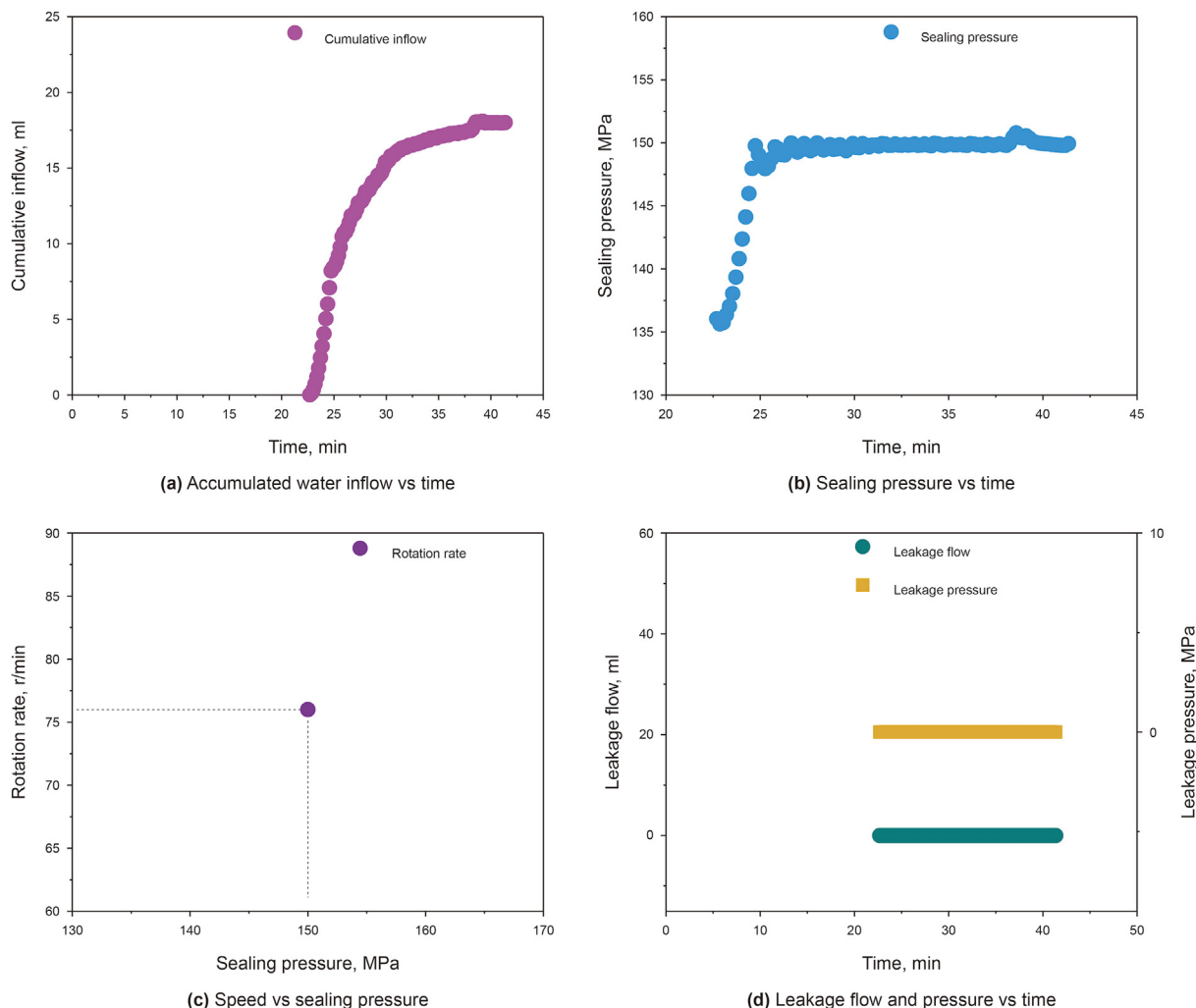
Fig. 15. Experimental parameters and result curves (maximum sealing pressure of 150 MPa; rotating speed of 76 r/min).

that the depth of the oil groove also decreases, resulting in the reduction of the volume of the oil groove. It is suggested that the reduction of the depth of the oil groove be used to quantitatively predict the service life of the sealing ring.

6.1.2. Three-dimensional scanning topography analysis of the water pressure surface

The water pressure surface is the part where the "Z" type ring of the combined sealing ring is in contact with high-pressure water. A three-dimensional scanner was used to obtain the meso-surface shape photos of the hydraulic surface, as shown in Fig. 17.

Based on the experimental photos, a typical area was selected to calculate the meso parameters, and the Formula is shown in (10) ~ (12). The calculated results are shown in Table 8.

As can be seen from Table 8, the roughness S_a of the water pressure surface before the experiment is 2.645 μm, and after the experiment, it is 2.632 μm, that is, the roughness of the water pressure surface of the sealing ring almost does not change before and after the experiment, indicating that there is no obvious sliding friction on the water pressure surface. This is because the high-pressure water is mainly exposed to the compressed effect, on the water pressure surface extrusion pressure, rather than friction. Therefore, the water pressure surface is not damaged by friction due to the change of the surface roughness shape.

However, physical observations of the sealing ring show no obvious wear in the transition position between the water pressure surface and the main sealing surface. This is because this position is affected by fluctuations in the process of contact and friction between the main sealing surface and the rotation axis under ultra-high water pressure. Therefore, in the maintenance of this device, attention needs to be paid to the wear condition of this position. Observing the wear at this position can serve as another way to predict the life of the sealing ring.

6.2. Microstructure analysis of the main sealing surface and the water pressure surface

Scanning electron microscopy (SEM) can be used to observe the microscopic structure of materials (Feng et al., 2019; Wu et al., 2020; Huang et al., 2021; Zhu et al., 2021; Wang et al., 2021). Therefore, SEM was used in this study to scan the microstructure of the main sealing surface and the water pressure surface of the "Z" ring, and the scanning images before and after the test were compared and analyzed to study the micro-wear condition and mechanism of the sealing ring structure during the experiment. Due to the large number of photos obtained by SEM observation and the limited length of this paper, only a few representative SEM pictures are presented for the micro-view analysis of the main
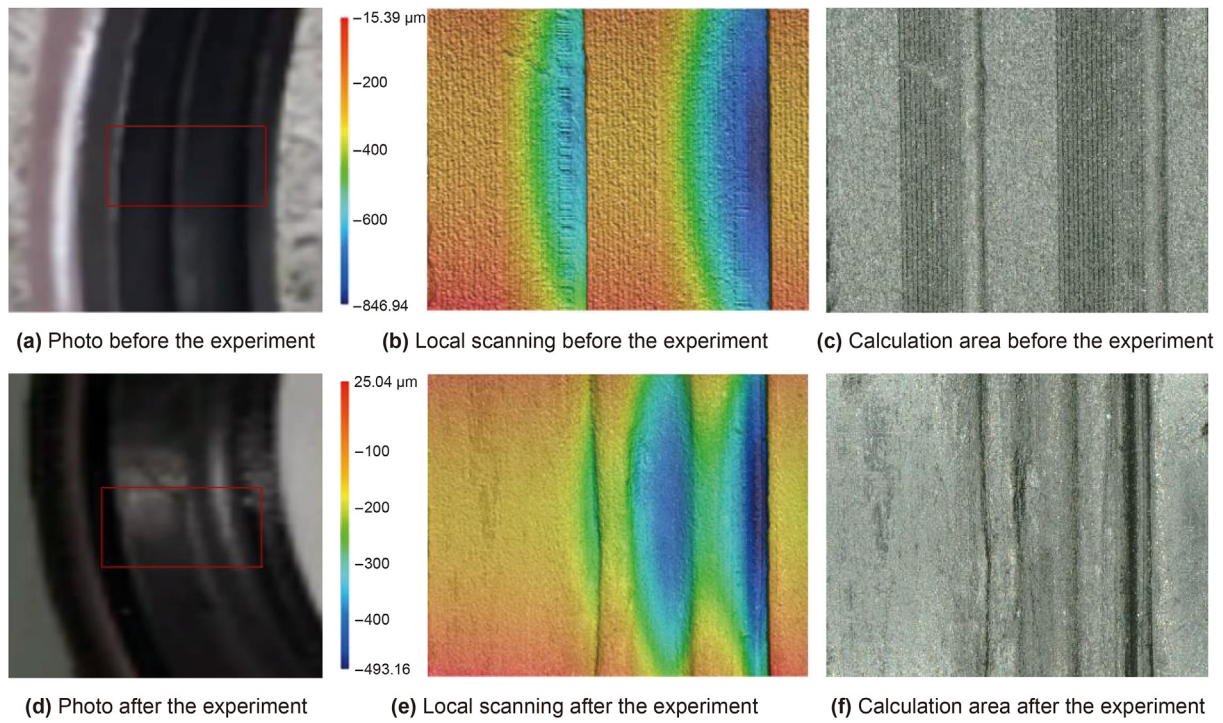
(a) Photo before the experiment

(b) Local scanning before the experiment

(c) Calculation area before the experiment

(d) Photo after the experiment

(e) Local scanning after the experiment

(f) Calculation area after the experiment

Fig. 16. 3D morphology of the main sealing surface before and after dynamic sealing test.

Table 7
Main surface shape evaluation parameters.

Parameters	S_a, μm	S_z, μm	S_{tr}	S_{pc}, 1/mm
Before the experiment	6.925	41.675	0.335	46.683
After the experiment	1.945	13.000	0.373	13.181

sealing surface and the water pressure surface.

6.2.1. Microstructure analysis of the main sealing surface

Comparing the SEM images shows that the main sealing surface before the experiment was rough with obvious bulges, as shown in
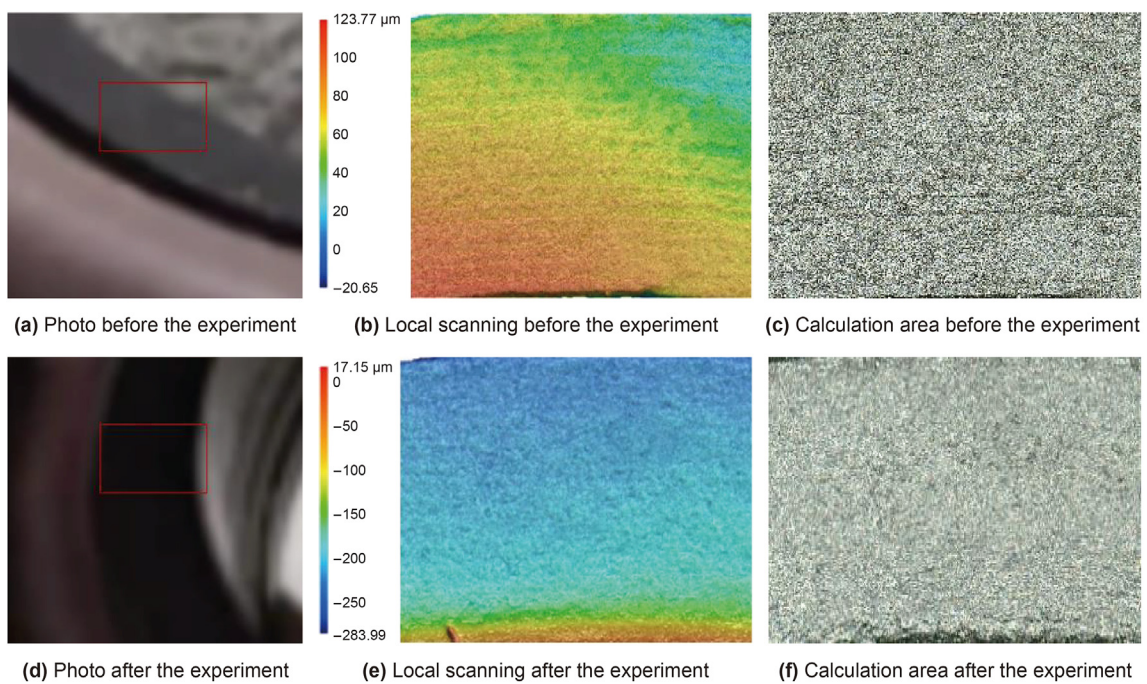

(a) Photo before the experiment

(b) Local scanning before the experiment

(c) Calculation area before the experiment

(d) Photo after the experiment

(e) Local scanning after the experiment

(f) Calculation area after the experiment

Fig. 17. 3D morphology of the hydraulic surface before and after the dynamic seal test.

Table 8
Main surface shape evaluation parameters.

Parameters	S_a, μ m	S_z, μ m	S_{tr}	S_{pc}, 1/mm
Before the experiment	2.645	18.567	0.190	16.941
After the experiment	2.632	21.067	0.186	16.421

Fig. 18(a). After the experiment, the sealing surface is smooth on the whole, and the contour of the main sealing surface is flattened, as shown in Fig. 18(b)~(d). The microscopic contour of the sealed oil groove surface has clear stripes before the experiment, while there are no obvious stripes on the oil groove surface after the experiment. All these are due to the surface polishing phenomenon caused by the contact between the main sealing surface and the high-speed rotating axis during the experiment, which makes the surface smooth. Observations of the main sealing surface after all the experiments show that micro-pore cracks developed in a few areas along with some detrital spalling, as shown in Fig. 18(e). However, the overall structure on the upper surface was still smooth and compact, without obvious structural defects. Further observation also revealed a transverse strip microstructure on the

main sealing surface after the test, and the horizontal strip extended along the circumference, as shown in Fig. 18(f). The reason for this is that in the test process, the main sealing surface attained a high temperature due to friction, which led to the softening of the surface material. The high-speed rotation of the rotation axis drives the softened material to flow along the circumferential direction to form a horizontal strip structure.

6.2.2. Microstructure analysis of the water pressure surface

Fig. 19 shows the SEM images of the water pressure surface of the "Z"-shaped ring. Comparing the scanning results before and after the test shows that the microscopic geometric contour shows no obvious flattening. However, some signs of wear appeared in some areas of the water pressure surface after the test, as shown in Fig. 19(d). The reason for this is that in the test process, the water pressure surface of the "Z" ring was subjected to ultra-high water pressure, and the water pressure generated small fluctuations due to the rotation of the rotation axis, which resulted in the erosion of the water pressure surface of the "Z" ring. However, the erosion is only local and very shallow. Overall, the structure of the hydrostatic surface after the experiment was observed to be compact with no trace of structural damage.
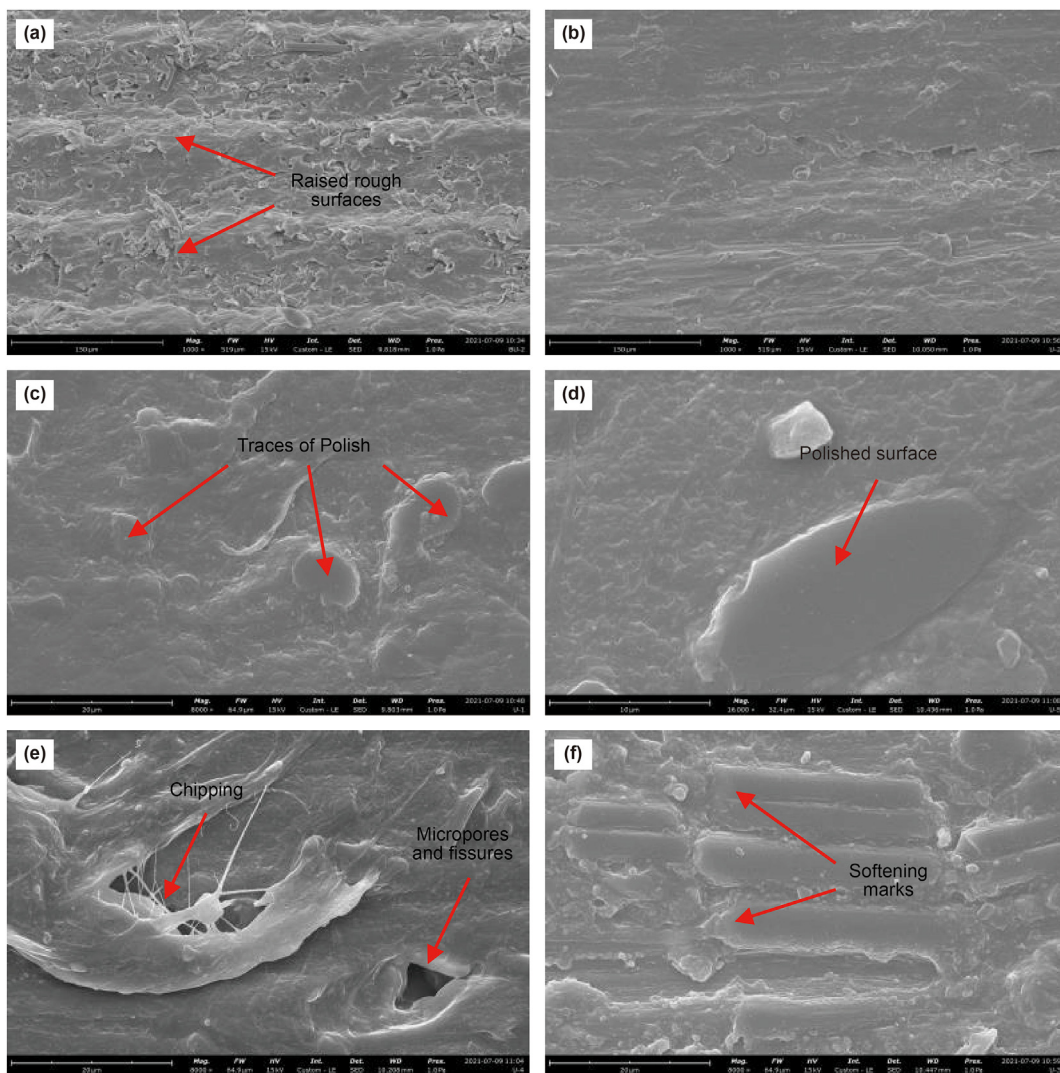

Fig. 18. The microstructure of the main sealing surface before and after the experiment ((a) is the main sealing surface before the experiment; (b)~(f) are the main sealing surfaces after the experiment.
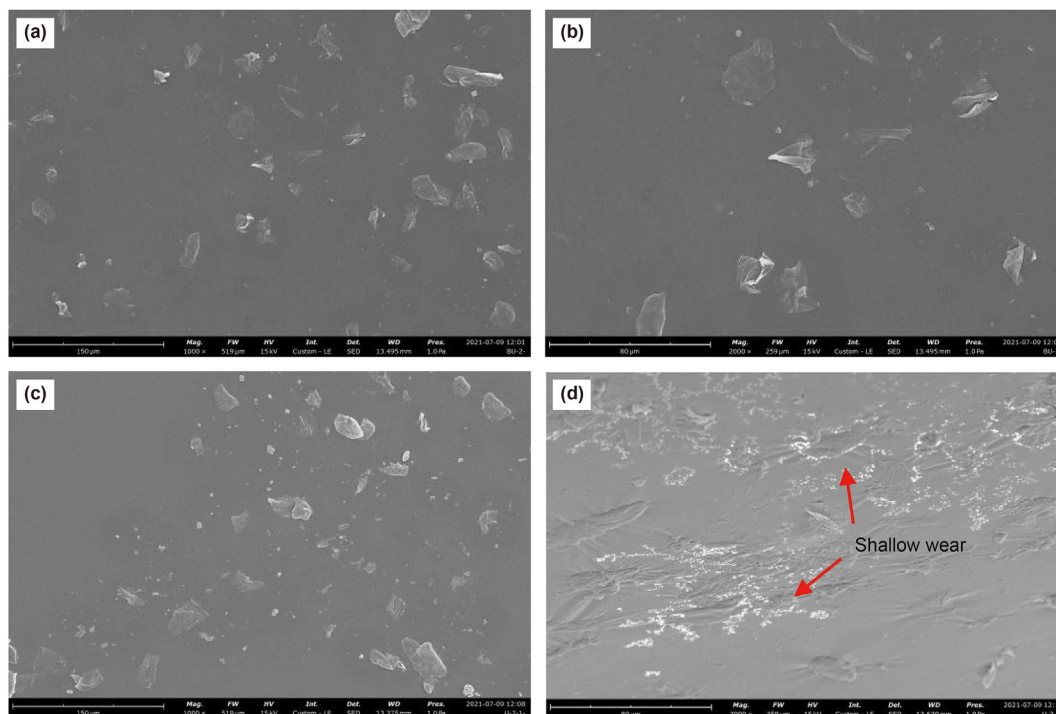
Fig. 19. Microstructure ((a) and (b) are before experiment; (c) and (d) are after the experiment.).

Although a few micro-pore cracks developed after the experiment, no obvious structural damage was observed. Therefore, on the whole, the sealing ring is durable. However, in the structural design of ultra-high-pressure rotary combined seals, it is still necessary to pay attention to the wear of the oil grooves and other defects. In use, it is also necessary to regularly detect these damages to maximize the safety and reliability of the seal.

7. Conclusion

In this study, a rotary combined dynamic seal and an experimental system to test its performance test were developed. Performance tests of the ultra-high-pressure rotating combined dynamic seal structures were carried out under different pressures and rotating speeds. The main conclusions are as follows:

(1) The ultra-high-pressure rotating combined dynamic seal structure can operate stably under a rotating speed of up to 140 r/min and a sealing pressure of up to 120 MPa; it can also operate stably under a pressure of up to 150 MPa and a rotating speed of up to 76 r/min.
(2) During the operation of the ultra-high-pressure rotating combined dynamic seal, the sealing ring gradually becomes smooth while the depth of the oil groove becomes shallow, which affects the lubrication. Therefore, the reduction in the oil groove depth can be used to predict the normal service life of the sealing ring. The roughness of the water pressure surface is not affected by the operation of the sealing structure.
(3) After the dynamic sealing experiment, a few microcracks were observed on the main sealing surface; this was caused by the local temperature rise caused by the repeated friction between the rotating shaft and the sealing ring at relatively high speed combined with repeated mechanical force impacts. However, these micro-pore cracks only appear in small

areas locally. Overall, the microscopic structure of the sealing ring is compact and complete, and there is no obvious structural damage. The sealing ring in normal operation can better maintain its sealing reliability. Even so, in the future, the cumulative use of sufficiently lengthy experiments or long time use of the dynamic seal will cause increasingly more obvious wear on the sealing structure. Therefore, great attention still needs to be paid to the wear of the main sealing surface of the sealing ring.

In the sealing performance test experiment of the dynamic seal structure designed in this study, no pressure and flow leakages were detected in the entire process. Therefore, the sealing performance of the device is intact.

References

Blasiak, S., Laski, P.A., Takosoglu, J.E., 2013. Parametric analysis of heat transfer in non-contacting face seals. Int. J. Heat Mass Tran. 57 (1), 22–31. https://doi.org/10.1016/j.ijheatmasstransfer.2012.09.058.
Chen, B., Yang, X., Tu, Q., 2019. The sealing performance of cap-shape ring combined seal. Lubric. Eng. 44 (3), 92–98 (**in Chinese**).
Chen, J., Cai, W., 2019. Effect of scratching frequency on the tribocorrosion resistance of Al-Mn amorphous thin films. Wear 1457–1465. https://doi.org/10.1016/j.wear.2018.12.055.
Chen, H., Liu, J., Ren, K., et al., 2016. Optimization of upstream pumping mechanical seal based on response surface method. J. Drain. Irrigation Mach. Eng. 34 (3), 232–237 (**in Chinese**).
Cheng, D.S., 2010. Handbook of Mechanical Design. Chemical Industry Press (in Chinese).
Feng, G., Kang, Y., Meng, T., et al., 2017. The influence of temperature on mode I

fracture toughness and fracture characteristics of sandstone. Rock Mech. Rock Eng. 50 (8), 2007–2019. https://doi.org/10.1007/s00603-017-1226-y.

Feng, G., Kang, Y., Sun, Z.D., et al., 2019. Effects of supercritical CO_2 adsorption on the mechanical characteristics and failure mechanisms of shale. Energy. https://doi.org/10.1016/j.energy.2019.02.069.

Gao, M.Z., Liu, J.J., Lin, W.M., et al., 2020a. Study on in-situ stress evolution law of ultra-thick coal seam in advance mining. Coal Sci. Technol. 48 (2), 28–35(in Chinese).

Gao, M.Z., Wang, M.Y., Xie, J., et al., 2020b. In-situ disturbed mechanical behavior of deep coal rock. J. China Coal Soc. 45 (8), 2691–2703 (in Chinese).

Gao, M.Z., Xie, J., Gao, Y.N., et al., 2021a. Mechanical behavior of coal under different mining rates: a case study from laboratory experiments to field testing. Int. J. Min. Sci. Technol. 31 (2021), 825–841. https://doi.org/10.1016/j.ijmst.2021.06.007.

Gao, M.Z., Xie, J, Guo, J, 2021b. Fractal evolution and connectivity characteristics of mining-induced crack networks in coal masses at different depths. Geomech. Geophys. Geo-Energy Geo-Resour. 7 (1). https://doi.org/10.1007/s40948-020-00207-4.

Gao, M.Z., Zhang, J.G., Li, S.W., et al., 2020c. Calculating changes in the fractal dimension of surface cracks to quantify how the dynamic loading rate affects rock failure in deep mining. J. Cent. S. Univ. Technol. 27 (10), 3013–3024. https://doi.org/10.1007/s11771-020-4525-5.

Guo, Y., Wu, L., Xu, H., et al., 2021. Analysis of dynamic sealing performance of Glyd ring and optimization of sealing parameters. Lubric. Eng. 46 (3), 17–25 (**in Chinese**).

Han, Z.J., 2019. Study on Wear Morphology Analysis and Optimization of Rotary Seal in Deep Well. Southwest Petroleum University (**in Chinese**).

He, Z.Q., Chen, L., Liu, T., et al., 2019. The optimization of pressure controller for deep earth drilling. Therm. Sci. 23 (3), 877–885. https://doi.org/10.2298/TSCI180612123H.

Huang, D.C., Xie, G., Peng, N.Y., et al., 2021. Synergistic inhibition of polyethylene glycol and potassium chloride in water-based drilling fluids. Petrol. Sci. 18, 827–838. https://doi.org/10.1007/s12182-020-00543-w.

ISO, Iso 25178-2, 2012. Geometrical product specifications (GPS)-Surface texture: areal Part 2: terms, definitions and surface texture parameters. Available from: http://www.iso.org.

Khedkar, J., Negulescu, I., Meletis, E.I., 2002. Sliding wear behavior of PTFE composites. Wear 252 (5–6), 361–369. https://doi.org/10.1016/S0043-1648(01)00859-6.

Mo, L., Wang, J., Guan, X.Q., 2014. Analysis of dynamic sealing characteristics of O-ring in petroleum machinery. Chin. Petrol. Mach. 42 (1), 103–107 (**in Chinese**).

Mooney, M.A., 1940. Theory of large elastic deformation. J. Appl. Phys. 11 (9), 582–592. https://doi.org/10.1063/1.1712836.

Nikas, G.K., Sayles, R.S., 2006. Computational model of tandem rectangular elastomeric seals for reciprocating motion. Tribol. Int. 39 (7), 622–634. https://doi.org/10.1016/j.triboint.2005.04.004.

Rivlin, R.S., 1997. Large Elastic Deformations of Isotropic Materials. https://doi.org/10.1007/978-1-4612-2416-7_6.

Salant, R.F., Maser, N., Bo, Y., 2007. Numerical model of a reciprocating hydraulic rod seal. Trans.Asme J.Tribol . 129 (1), 577–583. https://doi.org/10.1115/1.2401222.

Sukumar, T., Subramanian, M., Subramaniyan, S.K., et al., 2015. Design and Optimization of Lip Seal for Air Braking System. https://doi.org/10.4271/2015-26-0215.

Toki, S., Che, J., Rong, L., et al., 2013. Entanglements and networks to strain-induced crystallization and stress–strain relations in natural rubber and synthetic polyisoprene at various temperatures, pp. 5238–5248. https://doi.org/10.1021/ma400504k, 46(13).

Wang, Z.Z., Njiekak, G., Schmitt, D.R., et al., 2021. Empirical rock physics relationships on carbonate dry-frame elastic properties. Petrol. Sci. 18, 783–806. https://doi.org/10.1007/s12182-021-00565-y.

Wu, D.F., Guan, Z.W., Cheng, Q., et al., 2020. Development of a friction test apparatus for simulating the ultra-high pressure environment of the deep ocean. Wear 203294. https://doi.org/10.1016/j.wear.2020.203294.

Wood, R.J.K., 2017. Marine wear and tribocorrosion. Wear 893–910. https://doi.org/10.1016/j.wear.2017.01.076.

Xie, H.P., 2019. Special issue "deep mining.". Rock Mech. Rock Eng. 52, 1415–1416. https://doi.org/10.1007/s00603-019-01805-9.

Xie, H.P., Gao, F., Ju, Y., 2015. Research and development of rock mechanics in deep grand engineering. Chin. J. Rock Mech. Eng. 34 (11), 2161–2178 (**in Chinese**).

Xie, H.P., 2017. Research framework and anticipated results of deep rock mechanics and mining theory. Adv. Eng. Sci. 49 (2), 1–16 (**in Chinese**).

Xie, H.P., Liu, T., Gao, M.Z., et al., 2021. Research on in-situ condition preserved coring and testing systems. Petrol. Sci. https://doi.org/10.1016/j.petsci.2021.11.003.

Yin, Q., Wu, J.Y., Zhu, C., et al., 2021a. Shear mechanical responses of sandstone exposed to high temperature under constant normal stiffness boundary conditions. Geomech. Geophys. Geo-Energy Geo-Resour. 7 (2), 1–17. https://doi.org/10.1007/s40948-021-00234-9.

Yin, Q., Wu, J.Y., Zhu, C., et al., 2021b. The role of multiple heating and water cooling cycles on physical and mechanical responses of granite rocks. Geomech. Geophys. Geo-Energy Geo-Resour. 7 (3). https://doi.org/10.1007/s40948-021-00267-0.

Zhao, L., Suo, S.F., Shi, J.W., et al., 2020. Design and research of high-pressure rotary combined seal test device. Lubric. Eng. 45 (12), 86–90 (**in Chinese**).

Zhao, Z.P., Xu, P.F., Cheng, H.X., et al., 2019. Impact fatigue behaviors of Ti6V4Al alloy under compressive and tensile stresses. Wear 217–222. https://doi.org/10.1016/j.wear.2019.03.017.

Zhu, X.H., Jing, Y., 2017. Analysis of main in fluence factors for slip ring combined rotating seals based on 3D contact. China Mech. Eng. 28 (13), 1548–1553 (**in Chinese**).

Zhu, M.L., Qian, H.J., Yuan, R.X., et al., 2021. EDTA interfacial chelation Ca^{2+} incorporates superhydrophobic coating for scaling inhibition of $CaCO_3$ in petroleum industry. Petrol. Sci. 18, 951–961. https://doi.org/10.1007/s12182-021-00558-x.